Accepted manuscript

Damage imaging algorithm for non-destructive inspection of CFRP/steel adhesive joints based on ultrasonic guided wave propagation

Erwin Wojtczak, Magdalena Rucka

In: *Composite Structures* 297, 115930

DOI: https://doi.org/10.1016/j.compstruct.2022.115930

Please cite this article as:

E. Wojtczak, M. Rucka, Damage imaging algorithm for non-destructive inspection of CFRP/steel adhesive joints based on ultrasonic guided wave propagation, *Composite Structures* 297 (2022) , 115930, doi: https://doi.org/10.1016/j.compstruct.2022.115930

Damage imaging algorithm for non-destructive inspection of CFRP/steel adhesive joints based on ultrasonic guided wave propagation

Erwin Wojtczak*, Magdalena Rucka

Department of Mechanics of Materials and Structures, Faculty of Civil and Environmental Engineering, Gdańsk University of Technology, Narutowicza 11/12, 80-233, Gdańsk, Poland,
emails: erwin.wojtczak@pg.edu.pl, magdalena.rucka@pg.edu.pl
* corresponding author

Abstract

The paper concerns assessing the quality of the adhesive connection between a steel plate and the reinforcing CFRP laminate. A three-stage algorithm for non-destructive damage imaging was developed. As the first step, an initial study involving dispersion curves of joint components was executed to determine the material parameters and the appropriate excitation frequency. During the second step, damage identification in three-layer joints was performed using the weighted root mean square (WRMS) of the guided wave signals. A novel approach to determine the optimal values of WRMS parameters was proposed. Within the third step, the guided wavefield was recorded by scanning laser vibrometry. Visualization of the distribution of WRMS values on the surface of scanned specimens allowed efficient damage imaging. The application of statistical analysis (histograms) was used to prepare the final damage maps. The results of the investigations showed the high usefulness of the developed approach for imaging both intentionally introduced and unintended defects in adhesive joints.

Keywords

Weighted root mean square (WRMS); Guided wave propagation; Non-destructive testing (NDT); Damage imaging; Carbon fibre reinforced polymer (CFRP); Adhesive joints

1. Introduction

Engineering structures experience many harmful factors that can adversely affect their performance during various stages of their life cycle. Natural ageing of materials, design mistakes, environmental conditions, vandalistic devastation, or accidental defects can lead to progressive damage or even structural failure. Strengthening of existing structures is an essential issue since it can eliminate the results of such destructive factors, providing the appropriate safety level and comfort of use. Nowadays, there are many methods of strengthening structures or their elements, depending on the type of structure. Being commonly used in mechanical and civil engineering, metal and concrete elements often require repair or retrofitting. The application of externally bonded reinforcement (EBR) is an efficient method of improving the mechanical features of structural elements with many efficient implementations in real structures. EBR can have a form of adhesively bonded plates, mainly made of steel or composites. Being lightweight and high strength materials, fibre reinforced polymers have many

applications in the strengthening of structural elements, e.g., steel beams [1,2], plates [3–5], pipes [6–9] or concrete beams [10–14].

One of the most commonly used materials for external strengthening is carbon fibre reinforced polymer (CFRP). Taking into account that the bonding of CFRP reinforcement requires the use of adhesives, it is crucial for the efficiency of strengthening to provide an adequate quality of the manufactured joint. It is essential to note that typical adhesive connections are not capable of being assessed via visual inspection since they are hidden between joined elements. Moreover, CFRP reinforcement is mainly a layered medium, thus internal delamination can occur without a possibility of visual detection. Since destructive tests can be expensive and cannot be applied in existing structures, it is preferable to adopt a non-destructive testing (NDT) approach. Many techniques can be applied for non-invasive diagnostics of adhesive joints and CFRP elements, among which, the literature shows several interesting studies involving guided wave-based techniques for NDT, reported below. An important feature of ultrasonic guided waves is that guided wavefields carry valuable information about anomalies due to interactions of waves with structural damages. Many researchers took the issue of ultrasonic wave-based damage detection in CFRP elements. Hosseini et al. [15] studied the modelling of ultrasonic Lamb wave propagation in honeycomb composites and CFRP plates. They proposed a new finite element for the analysis of nonreflecting waves. Martínez-Jequier et al. [16] investigated CFRP samples under three-point bending using the acoustic emission (AE) technique. They associated different damage mechanisms (delamination, fibre breaking, and matrix micro-cracking) with the characteristics of propagating wave modes. Detection of CFRP with barely visible impact damage was considered by Zhang et al. [17]. An ultrasound waveform distortion indicator was used to distinguish samples prepared with different impact energies. Sikdar and Banerjee [18] considered the localization of inhomogeneities in advanced sandwich composite structures based on changes in signal amplitudes. Duan and Gan [19] presented a theoretical investigation of the properties of waves propagating in anisotropic composite laminates, basing on the dispersion curves characteristics. Mesoscopic modelling of wave propagation in three-dimensional space using the finite element method was considered by Nakahata et al. [20]. They estimated the elastic parameters of CFRP composite using the inversion method and used them for comparison of experimental and theoretical guided wavefields. Apalowo and Chronopoulos [21] proposed a numerical scheme for quantifying wave interaction with structural damage in layered composites. They used periodic structure theory and finite element method to simulate wave propagation in order to detect and assess the orientation and extent of the defects. Sikdar et al. [22] took up the issue of nonlinear wave propagation in the presence of debonding with varying sizes between composite plates and stiffeners. They assumed the change of the amplitude of the second harmonic due to the debond size as a nonlinear indicator of the level of damage. James and Giurgiutiu [23] analyzed quasi-isotropic CFRP elements with barely visible impact damage. They linked the parameters of the impact test with the size of damage for plates with different thicknesses. Rozylo and Debski [24] analyzed composite profiles with a top-hat section under eccentric compressive loading.

They determined fast Fourier transform spectra of signals registered using the acoustic emission technique for the identification of delamination and fibre cracking in samples during loading.

The problem of damage identification in adhesive joints of structural elements was also considered. Mahmoud et al. [25] used surface acoustic waves for the non-destructive evaluation of CFRP strengthened concrete specimens under ageing conditions simulated as long-term water immersion at different temperatures. They correlated the wave characteristics with the fracture energy determined in destructive testing of the samples. Li et al. [26] considered the evaluation of debonding in concrete beams reinforced with CFRP plates. They proposed the determination of the severity of debonding as a damage index in the form of a correlation coefficient between an actuated wave signal and a signal received at a specific point of specimens. Liu et al. [27] applied ultrasonic waves for monitoring damage development in CFRP-strengthened concrete beams under bending test. They observed a decrease in signal amplitude and a change of time of flight of waves during progressing damage. Wang et al. [28] considered the detection of damage at the interface between a concrete column and an adhesively bonded CFRP overlay using guided waves. They identified intentional defects and monitored the debonding of the sample under bending load. Kwon and Lee [29] evaluated adhesively bonded CFRP-aluminium lap joints with different types of artificial defects. They considered the wave propagation induced by different pulse signals and tone bursts with different frequencies to obtain an optimal one. Li et al. [30] analyzed the propagation of antisymmetric wave modes for damage detection in adhesive joints between steel plates and CFRP laminates. They observed a linear relationship between the time of flight of ultrasonic waves and the debonding size.

The above-reported literature shows that damage detection in CFRP lamina and CFRP strengthened elements is a widely analysed topic. It is, however, important to note that most of the researchers did not consider the visualization of actual damage areas. Some studies involving guided waves for visualization of the actual shape and position of defects in particular structural elements are reported below. Spytek et al. [31] inspected adhesively bonded aluminium plates with artificial defects produced with Teflon layers. The laser ultrasound system was used for the investigation of zero-group velocity modes of Lamb waves in the case of damage visualization based on frequency spectrum characteristics. Damage visualization in CFRP plate and honeycomb sandwich panels was considered by Sha et al. [32]. They proposed using guided wavefield curvature, stating that it is more sensitive to defects than the wavefield itself. A simple and efficient damage imaging technique based on vibration energy distribution utilizes the calculation of a root mean square (RMS) or, more advanced, its weighted variant (WRMS). Żak et al. [33] considered aluminium and composite elements with damage in the form of an additional mass. They provided visualization based on WRMS calculations of waves collected using a scanning laser Doppler vibrometer (SLDV). WRMS was also used for the investigation of notches and corrosion in aluminium plates by Lee et al. [34,35]. The presence of disbond inserts in composite elements was considered by Pieczonka et al. [36] with the use of a 3-D SLDV and RMS. An attempt to determine the optimal parameters of WRMS calculation was performed by Rucka et al. [37].

They used statistical analysis to establish an optimal weighting factor and time of averaging for the imaging of internal defects in adhesive joints of steel plates. An extension of this research was presented by Wojtczak and Rucka [38]. They focused on the determination of the optimal frequency of the excitation signal used for wave propagation measurements. Summarizing all the studies mentioned above, the WRMS-based visualization technique was used for some specimens made of different materials. However, the propagation of ultrasonic guided waves was not considered in layered media containing composite layers. What is also important, most of the studies did not discuss the problem of determination of optimal values of WRMS calculation parameters, they are usually set arbitrary with no clear explanation.

The aim of the study is damage visualization in adhesive joints between steel plates and external reinforcement in the form of CFRP lamina. Extensive research has been carried out on guided wave propagation in layered media containing a transversely isotropic layer. Theoretical and experimental dispersion curves were determined for each of the analyzed materials (steel, adhesive, CFRP), as well as for the three-layer joint. A set of carefully planned experiments was conducted for damage detection and visualization using the calculation of the WRMS of the recorded guided wave signals. The novel element of the research is the development of a three-stage procedure for non-destructive damage imaging in adhesive joints of engineering structures. The determination of optimal values of WRMS calculation parameters based on the linearization of the relationship between the increase of the WRMS value and the level of damage was proposed. The application of the WRMS histograms for the determination of the actual level of damage was suggested. The proposed approach was successfully verified by the experimental investigation of the joints after disconnection. The reported outcomes of the research allowed stating that the unsupervised choice of calculation parameters can significantly influence the efficiency of damage visualization, whereas the appropriate analysis of optimal parameters provides useful results.

2. WRMS-based algorithm for damage detection and imaging

In the current research, the conventional measurement methods (e.g., non-contact ultrasonic wave propagation scanning) and signal processing techniques (e.g., WRMS calculations) are arranged in a novel multi-stage procedure for non-destructive damage imaging in adhesive joints of engineering structures. The scheme of the proposed algorithm is presented in Figure 1. The analysis can be divided into three steps. Before the major part of the study, some initial analyses need to be performed (step 1). Firstly, the dynamic elastic parameters of the materials used to prepare the specimens are determined. For homogeneous isotropic materials without viscous properties (e.g., steel), the dynamic Young's modulus such as dynamic Poisson's ratio can be assumed as equal to the static ones. Thanks to that, static tensile tests are sufficient to determine the required parameters. In the case of viscous materials (e.g., epoxy adhesive), the dynamic parameters can differ from the static ones, thus it is required to apply dynamic methods based on ultrasonic pulse velocity measurements or dispersion curves calculations. After determining the dynamic material parameters, dispersion curves can be calculated for the analyzed

specimens. Based on the differences in the dispersion relations of single- and multi-layer media, an appropriate excitation frequency can be determined.

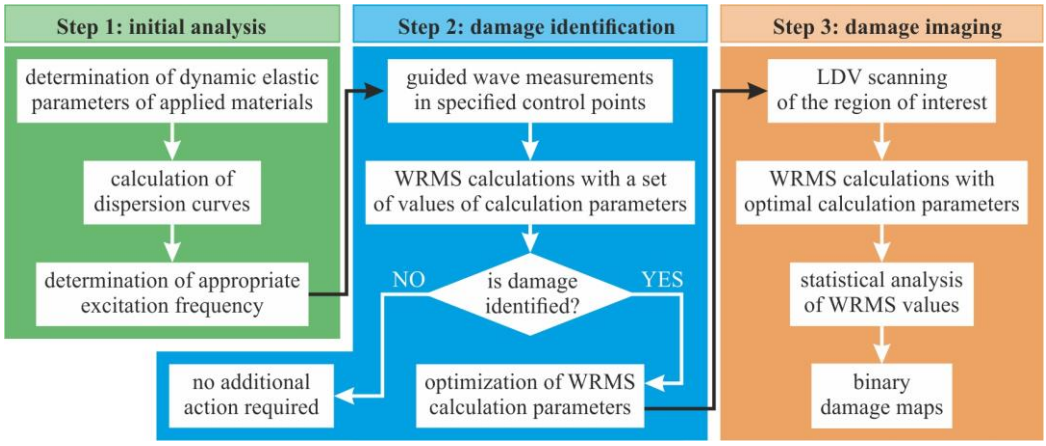

Figure 1. Scheme illustrating the proposed procedure for non-destructive damage imaging in adhesive joints of engineering structures using guided wave propagation and WRMS calculations

The second step of the algorithm (step 2) is focused on the identification of defects. Firstly, the guided waves are excited and collected in a small number of control points placed in specific locations of the analysed specimen. Subsequently, the WRMS values are calculated for the collected signals, using a few heuristically set values of the calculation parameters. The comparison of WRMS values in control points allows determining the presence of damage. If no visible change of WRMS is observed, the algorithm finishes with no further operation required. If, however, an increase of WRMS is revealed, the defect is identified. In this case, the determination of WRMS calculation parameters is performed to efficiently visualize the damaged regions in further steps. Two-parameter optimization can be performed, including variation of time of averaging and weighting factor. In the current paper, the determination of optimal WRMS calculation parameters is done based on the linearization between WRMS value in control points and the size of the defect. It is, however, important to note that the proposed algorithm can be further developed with the use of different optimization approaches.

Having determined an appropriate excitation frequency and WRMS optimal calculation parameters, the final step of the analysis can be made, i.e., damage imaging (step 3). Firstly, the guided wave propagation measurements at multiple points in the specific region of interest are performed. The use of an automated experimental setup, such as SLDV is beneficial to minimize the time cost. Based on the collected signals, the WRMS maps can be determined in the way of calculations performed with the optimal parameters determined in the previous step. Then, the statistical analysis of the set of WRMS values is engaged. The fact that the WRMS histogram for damaged joints shows a bimodal distribution is used to determine the mode WRMS values in the area of good adhesion and damage. Based on the differentiation between these two, the limit WRMS value is established. This threshold is then used to apply a binary scheme of determination of damage maps. Each point with the WRMS value above the limit is denoted as ‘one’, whereas all remaining points are denoted as ‘zero’. This allows showing the exact position and size of damage regions in the joint.

3. Materials and Methods

3.1. Object of investigation

The objects of the investigation were adhesive joints of steel plates and composite external reinforcement joined together by the adhesive. The specimens were as follows: an intact one (#0) and five with different levels of damage (10%, 20%, 50%, 80% and 100%, #1 – 5, consecutively; specimen #5 is a completely separated composite), modelled as a lack of adhesive. The geometry of the joints is presented in Figure 2. The steel plates of dimensions 500 mm × 100 mm were manufactured from structural steel of type S355 with a thickness of 11.9 mm. The composite was a pultruded carbon fibre reinforced polymer (CFRP) CarboDur® manufactured by Sika®. This high-strength unidirectionally reinforced laminate, consisting of carbon fibres and epoxy resin matrix, is intended for the external strengthening of structures. The applied laminate type S1012 had a width of 100 mm and a thickness of 1.24 mm. CFRP plates were bonded to the steel plates using a two-component epoxy resin SikaDur 30 Normal (Sika®) as a bonding agent. The resulting thickness of the adhesive film was equal to about 2 mm. The defects were obtained by introducing a layer of polystyrene sheeting with a thickness equal to the destined adhesive film in the destined regions. The inserts were removed during the preparation process, before the hardening of the epoxy. The prepared joints were cured at room temperature for seven days.

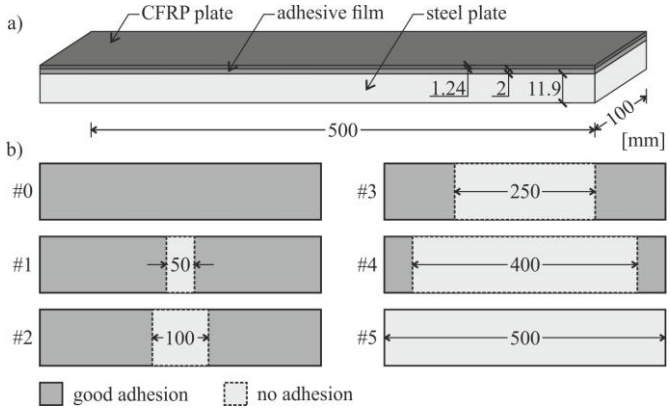

Figure 2. The geometry of analysed joints (a) with the variants of damage #0 – #5 (b)

In addition to specimens #0 – #5 intended for damage detection, several samples were prepared to determine material parameters. Firstly, a set of samples were prepared for static tests, i.e., five steel flat bars with dimensions of 200 × 20 × 11.9 mm (set #A), nine adhesive dogbone specimens with a global size of 200 × 30 × 3 mm (set #B) and three groups of specimens made of CFRP laminate (four coupons in each group) cut in three directions: along the fibres (#C), across the fibres (#D), and skew (#E), with an angle of 45 degrees, all with the dimensions of 100 × 20 × 1.24 mm. Secondly, a single plate for dispersion curves measurements was prepared for each material. Steel (#F) and CFRP (#H) plates had dimensions of 500 × 100 mm and differed only in thickness (11.9 and 1.24 mm, respectively), whereas the adhesive specimen (#G) had dimensions of 200 × 100 × 2.1 mm. The maerial densities of the materials were: ρ_s = 7582 kg/m^3 (steel), ρ_a = 1720 kg/m^3 (adhesive), and ρ_c = 1597 kg/m^3 (CFRP).

3.2. Experimental setup

3.2.1. Static tensile tests

Material properties of steel, CFRP and adhesive were identified in static tensile tests. Steel bars were examined using Zwick/Roell Z100 testing machine equipped with a contacting extensometer makroXtens II WN (Zwick, Germany). The experiments were performed with a constant displacement increment of 0.2 mm/min. From the test, the static Young's modulus was determined. Adhesive dogbone specimens and CFRP bars (rectangular specimens) were tested with Zwick/Roell Z10 machine supported with an optical videoXtens extensometer (Zwick, Germany), allowing determination of both the static Young's modulus and the Poisson's ratio. The tests were also displacement-controlled with the same test speed of 0.2 mm/min.

3.2.2. Guided wave propagation measurements

The measurements of guided waves were carried out by the scanning laser Doppler vibrometry (SLDV) technique. The experimental setup, shown in Figure 3a consisted of the laser vibrometer PSV-3D-400-M (Polytec GmbH) equipped with a VD-07 velocity decoder, the arbitrary function generator AFG 3022 (Tektronix, Inc.) and the high-voltage amplifier PPA 2000 (EC Electronics). The Lamb waves were excited employing the plate piezoelectric actuator NAC2024 (Noliac) with dimensions of $3 \times 3 \times 2$ mm^3, bonded to the specimen surface by petro wax 080A109 (PCB Piezotronics, Inc.). Each specimen was laying freely on the surface of a table top during measurements. It is important to note, that wave propagation was not disturbed by the environmental factors providing that no coupling between contacting surface of the specimen and table top was introduced.

Four samples (additional steel #F, adhesive #G and CFRP #H plates and intact joint #0) were at first tested to determine the dispersion curves. The guided wave signals were registered in 91 points distributed evenly along a straight line with a length of 90 mm. CFRP plate and joint #0 were measured along two paths, as depicted in Figure 3a: trace L along the fibre direction and trace T at an angle of 90° to the fibres. The measurements on joint #0 were conducted on both sides (at CFRP and steel surfaces). Steel and adhesive were assumed as homogeneous isotropic materials, therefore the measurements were performed only along a single trace (here, T). The PZT actuator was attached at position A1 for measurements along trace L, and at position A2 for measurements along trace T (Figure 4b). The excitation was a single-cycle sine wave modulated by the Hann window with a voltage of 2 V (peak to peak amplitude). Measurements along each trace were conducted five times with different carrier frequencies of the tone burst, namely, 50, 100, 150, 200, and 250 kHz. Each of the measured signals was averaged 20 times to improve the signal-to-noise ratio.

At the second stage, samples #0 to #5 were scanned in the context of damage detection and imaging. The excitation signal was a five-cycle wave packet obtained by Hann windowing of a sinusoidal burst with a central frequency of 100 kHz. Taking into account the damping of adhesive the peak to peak amplitude was increased to 5 V. The wave was excited by the PZT actuator attached at position A3 (Figure 4c). Guided wave signals were collected in 2829 points distributed on the top surface

of the CFRP plate, in a regular square grid with size 23×123, as shown in Figure 3c. The signals were averaged 20 times. To exclude the boundary regions from measurements, the margins of 6 mm were assumed, thus the area of scanning covered a surface of 488 × 88 mm^2, resulting in a scan resolution of 4 mm in both directions. In the case of potential damage identification (discussed further), two control points were marked (P1 and P2). The complete set of experimental data gathered by the laser vibrometer in the course of the guided wave measurements is available at [39].

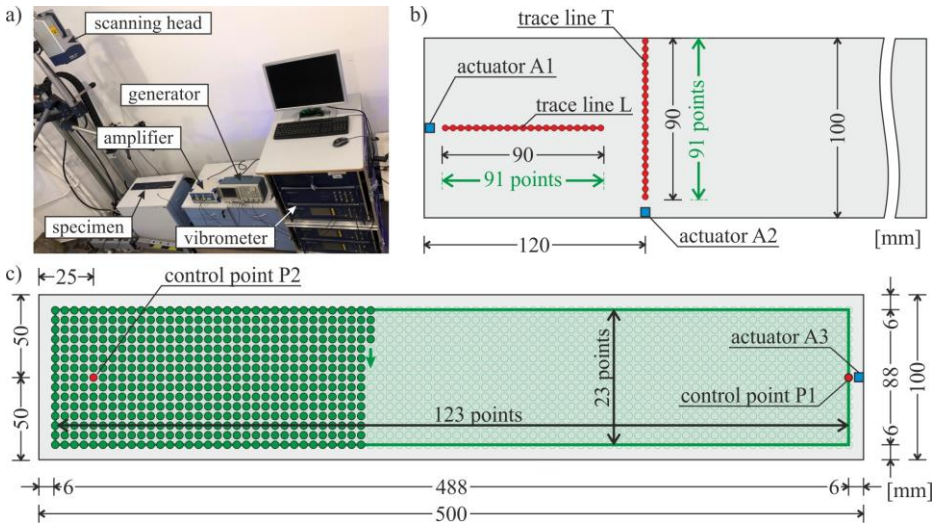

Figure 3. Scanning laser vibrometry for guided wave measurements: a) experimental setup; b) scheme of measurement traces for dispersion curves determination; c) scheme of measurement grid for damage imaging

3.3. Dispersion curves for isotropic and transversely isotropic materials

3.3.1. Theoretical calculations

Guided waves are a specific type of acoustic wave that propagates in restrained media. In elements bounded by two parallel surfaces (plate-like structures), so-called Lamb waves and shear horizontal waves can exist, mutually referenced as plate waves. Both wave types are naturally decoupled, which is because Lamb waves originate from pressure and shear vertical bulk waves, whereas shear horizontal guided waves stem independently from the shear horizontal bulk waves [40]. There are two considerably relevant features of guided waves, in general. The first one is multimodality which means that for a specific frequency value, many different modes can propagate independently in the analysed medium. Two types of Lamb wave modes can be observed: symmetric (S0, S1, S2,…) and antisymmetric (A0, A1, A2,…), and also shear horizontal waves can occur in symmetric (SH0, SH2,…) and antisymmetric (SH1, SH3,…) forms. The second important issue is the dispersive nature of guided waves which means that wave characteristics (like wavenumber, wavelength, and propagation velocities) are frequency-dependent. Dispersion curves constitute the graphical representation of these relations and their shapes are sensitive to changes in material parameters and geometry of the analysed medium. In the case of plate waves, the thickness of the plate, material density, and elastic parameters are important features. The complexity of the problem of dispersion curves determination depends on the type of analysed medium and the assumed method of modelling. In general, the relation between wavenumber k and

angular frequency ω is found. The simplest example is a homogeneous isotropic plate with a constant thickness. The dispersion relations can be determined independently for symmetric and antisymmetric Lamb wave modes by solving the so-called Rayleigh-Lamb equations [41–43].

In composite materials, the directional dependence of material properties creates the problem of dispersion curves calculation much more complex. Some complications correspond to the determination of mechanical parameters. A unidirectional fibre-reinforced lamina can be modelled as a transversely isotropic medium, for which at least five independent elastic constants need to be determined to build the stiffness matrix tensor **C** [44]. Denoting the fibre direction (symmetry axis) as 1 and the remaining directions as 2 and 3 (constituting plane of symmetry), one needs to determine two Young's moduli: along fibres E_1 and across fibres E_2, two Poisson's ratios: out of the plane of isotropy ν_{12} and in the plane of isotropy ν_{23}, and shear modulus out of the plane of isotropy G_{12}.The remaining constants are the dependent ones. Four of five constants can be easily determined in simple static tensile tests (E_1, ν_{12}, E_2, and G_{12}). According to the literature [45], some simplifications can be made to reduce the number of constants from five to four using the assumption that Poisson's ratio in the plane of symmetry is equal to Poisson's ratio in the transverse plane, i.e. $\nu_{23} = \nu_{12}$. Having the complete set of mechanical parameters it is possible to determine the stiffness tensor **C** as the inverse of a compliance tensor **S** which has a much more simple form. The determined stiffness tensor is used to calculate the theoretical dispersion curves. The literature provides some solutions to the dispersion problem for transversely isotropic and generally anisotropic media [46]. It is, however, beneficial to use the semi-analytical finite element method (SAFE) which assumes the discretization of the waveguide in the cross-section altogether with the adoption of an analytical solution in the wave propagation direction [43]. A simple and very effective software utilizing SAFE is GUIGUW [47]. The use of SAFE methods is very convenient also for layered media, especially consisting of non-isotropic layers.

3.3.2. Experimental measurements

The procedure of determination of experimental dispersion curves for a specific element is based on a series of measurements of propagating waves in points distributed along the line traced on the object surface (cf. Section 2.2.2 and Figure 3b). As a result, a guided wave field $s(x,t)$ in the space-time (x-t) domain is obtained. To improve the resolution of the desired dispersion relations in the wavenumber domain, a zero-padding is applied to the raw data $s(x,t)$ in the space domain, obtaining the expanded data $s_e(x,t)$. The two-dimensional fast Fourier transform (2D-FFT) is then applied to the expanded signal set $s_e(x,t)$ to convert it to the wavenumber-frequency (k-f) domain according to the formula [48,49]:

$$D(k, f) = \int\int s_e(x,t) \mathrm{e}^{-i2\pi(kx+ft)} \mathrm{d}x\mathrm{d}t \,, \tag{1}$$

where $D(k,f)$ denotes the Fourier coefficients (wave amplitudes) in the wavenumber-frequency domain. The range of the effective frequency spectrum depends on the excitation frequency. To visualize the curves in a wider frequency range, the above-described algorithm can be repeated for several

measurements with excitation signals with different carrier frequencies. The final result is an aggregation of a series of maps $D_i(k,f)$.

3.3.3. Determination of dynamic mechanical parameters based on dispersion curves

The sensitiveness of the dispersion curves to any changes in the parameters of the analysed medium allows using them for non-destructive determination of the mechanical properties of materials. They can be a very useful tool, especially in the case when static tests cannot be applied. Dispersion relations were successfully used for parameter identification in composite elements [50–53] and adhesive [54]. In the current research, a method based on the comparison of theoretical and experimental curves was applied. The algorithm firstly requires the determination of experimental dispersion curves using 2D-FFT (see the previous chapter). Dispersion curves are then extracted from the wavenumber-frequency field by tracing the peak values for a set of consecutive frequencies in the analysed frequency range. As a result, the dispersion relations in the intended form of single curves can be plotted. Secondly, a set of theoretical dispersion curves are calculated in a probable range of parameters values. Finally, the experimental curves are compared with the theoretical ones, obtained for all combinations of parameters. For each comparison, the value of the residual sum of squares (RSS) is calculated based on the difference between N experimental k_e and theoretical k_t wavenumber values, according to the formula:

$$RSS = \sum_{i=1}^{N} \left(k_{e,i} - k_{t,i} \right)^2 . \tag{2}$$

To obtain an optimal pair of determined parameters, the minimization of the RSS function is required. To eliminate the problem with cumbersome units of RSS, it can be normalized to its maximum value obtaining RSSn. Assuming that there are two varying material parameters, e.g., Young's modulus E_i and Poisson's ratio v_j, the RSSn is represented by a two-dimensional field RSSn(i,j) in E-v domain. What is worth noting, a single curve, as well as multiple curves, can be considered at the same time.

3.4. Damage imaging using WRMS

It is commonly known that a raw guided wavefield (e.g., acquired using SLVD, like in Section 2.2.2) is not the best way to represent the image of potential damage. Further signal processing of the collected signals is required to reveal the actual shape and position of a defect. The simple but very robust approach is based on the calculation of the root mean square (RMS), also called the effective value. For damage detection and visualization, it is beneficial to use the weighted root mean square (WRMS) that allows enhancing results by the reduction of the incident part of the signals collected. The WRMS technique is based on signal energy distribution, thus it is sensitive to any changes in material stiffness and the presence of boundaries, which makes it very promising for damage detection. Taking into account a discrete time-domain signal $s_r = s(t_r)$ with N samples ($r = 1,2,\ldots,N$) registered with a constant time interval Δt, giving the duration of $T_e = (N-1)\Delta t$, the WRMS can be calculated as follows [33,55,56]:

$$WRMS = \sqrt{\frac{1}{N}\sum_{r=1}^{N} w_r s_r^2}\ , \tag{3}$$

where w_r denotes a weighting factor whose value is defined for any consecutive sample based on its number as:

$$w_r = r^m\ . \tag{4}$$

In the above formula, m is a nonnegative power of the weighting factor. If $m = 0$, the weighting factor is constant and equal to a unit, thus no weighting is applied to the signals and the formula (3) describes the simple RMS. The power m is one of the quantities that strongly influences the quality of damage visualization. The second one is the time of averaging T_e, i.e., the duration of the signal taken into account. It is worth noting that the use of statistical analysis in the interpretation of damage visualization using WRMS can be effectively applied [37,38]. It was proved that WRMS histograms can be useful in the assessment of the level of damage.

4. Results and Discussion

4.1. Dispersion curves

As the initial step (cf. Figure 1) for further damage detection analysis, the calculation and interpretation of dispersion curves for the joint was done. At the start, the dispersion relations for the three components (i.e., steel, adhesive, and CFRP) were investigated to check their material parameters for the appropriate calculation of dispersion curves for the joint. Steel was treated as an isotropic material, thus only two mechanical parameters were required. The static tensile tests (sample set #A) provided the value of Young's modulus equal E_s = 197.3 GPa with a standard deviation of 7.7 GPa and a coefficient of variation 3.9%. The Poisson's ratio was assumed to be ν_s = 0.30. The calculations of the dispersion curves were carried out using an authorial script prepared in Matlab® solving Rayleigh-Lamb equations. The experimental dispersion curves for steel plate #F were determined using 2D-FFT. Figure 4a presents the theoretical curves superimposed on the experimental result. The visual agreement of experimental and theoretical curves allows stating that static elastic parameters are appropriate for the modelling of wave propagation in the analysed steel plates.

The investigations for the adhesive were then conducted. It can be also modelled as an isotropic material, thus Young's modulus and Poisson's ratio were determined during the static tensile tests on adhesive dogbone specimens from set #B. The mean value of the static Young's modulus was equal to $E_{a,s}$ = 11.80 GPa with a standard deviation of 0.98 GPa and coefficient of variation 8.3%. The static Poisson's ratio was equal to $\nu_{a,s}$ = 0.38 with a standard deviation of 0.08 and a coefficient of variation equal to 21%. The determined static parameters were used to calculate the theoretical dispersion curves (Figure 4b, black dashed lines) that were compared with the experimental relations obtained from the investigation of plate #G. The significant inconsistency was observed due to the well-known fact that the dynamic parameters of materials with viscoelastic properties (such as adhesives) can be different from the static ones. The reason is the high strain ratio during dynamic load [54,57–59]. Thus, the

dynamic parameters were determined by two-parametric optimization, using the procedure utilizing RSS calculation, described in Section 2.3.3. A series of dispersion curves were calculated in the Young's modulus range of 11 – 16 GPa and Poisson's ratio range of 0.1 – 0.45 to be compared with the experimental S0 and A0 curves extracted from the 2D-FFT map. As a result, the optimal values of dynamic elastic parameters were obtained as: $E_{a,d}$ = 13.5 GPa and $\nu_{a,d}$ = 0.30. The increase of the Young's modulus is visible, which is a typical relation for viscous materials. The corrected theoretical curves (including the dynamic parameters) are presented in Figure 4b (white solid lines). The convergence of the experimental and theoretical approaches is now evident. This fact allows stating that the determined dynamic parameters are correct. What is worth noting, the A0 curve is clearly visualized while the S0 curve is moderately visible. This is due to the fact that the PZT actuator induced vibrations in the direction perpendicular to the plate surface.

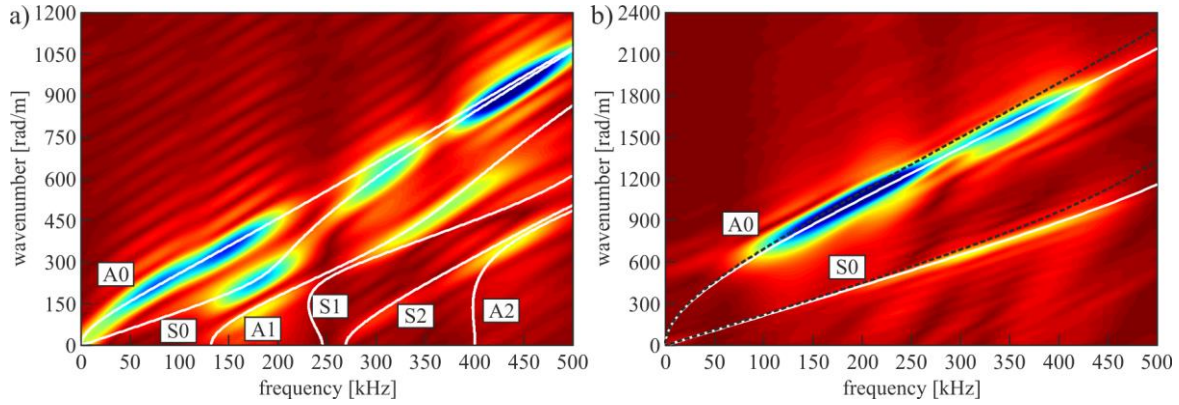

Figure 4. Dispersion curves for isotropic materials used in the study: a) experimental (coloured map) and theoretical (white line) curves for steel plate #F, b) experimental (coloured map) and theoretical curves (black dashed line and white solid line for static and dynamic parameters, respectively) for adhesive plate #G

The CFRP lamina needed to be analyzed as a transversely isotropic material, thus a number of parameters were determined in static tensile tests on samples from sets #C (E_1, ν_{12}), #D (E_2), and #E (E_{45} in the direction at a 45-degree angle). The obtained values are presented in Table 1 altogether with mean values, standard deviations, and coefficients of variation. Based on the determined constants, the shear modulus G_{12} in the transverse plane was calculated [44], giving a value of 6.73 GPa. The Poisson's ratio ν_{23} was assumed to be equal to ν_{12}. The theoretical dispersion curves for both directions 1 and 2 were calculated using GUIGUW software. The results are presented in Figure 5 with experimental curves determined along the corresponding L and T paths for plate #H (cf. Figure 3c). A good agreement of both fundamental modes is observed, which confirmed the appropriateness of the determination of elastic constants. According to the experimental relations, in L-direction curves, only the fundamental A0 mode is detected. The S0 mode was not detected, due to the antisymmetric character of the excitation. On the other hand, in T-direction both A0 and S0 modes are visible. The occurrence of S0 mode was possible because the propagation of the wave along T-direction was disturbed by the carbon fibres which constituted a significant heterogeneity.

Table 1. Static elastic parameters of CFRP lamina specimen sets #C, #D, #E

Parameter	MEAN	STD	COV
$E_{1,c}$ [GPa]	169.02	8.19	4.9%
$\nu_{12,c}$ [–]	0.503	0.050	9.9%
$E_{2,c}$ [GPa]	9.85	0.14	1.4%
$E_{45,c}$ [GPa]	15.99	1.23	7.7%

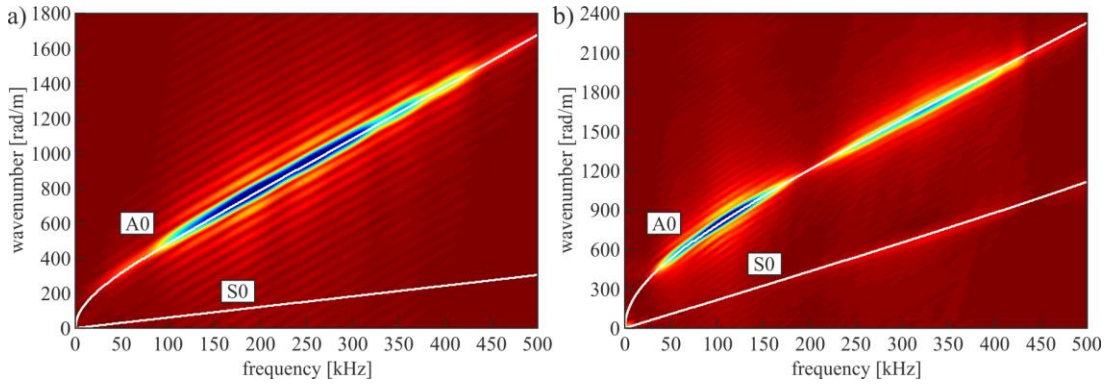

Figure 5. Experimental (coloured map) and theoretical (white line) dispersion curves for CFRP plate #H in two directions: a) L-direction; b) T-direction

As a final step in the dispersion relations analysis, the curves for the three-layer plate were determined using joint #0. The theoretical calculations were conducted with the use of GUIGUW software. The models were prepared based on the material parameters of steel, adhesive and CFRP. The experimental curves were determined for the signals registered on both upper and lower surfaces of joint #0 (on the steel and CFRP sides). The theoretical curves were superimposed on the experimental relations in Figure 6 for both directions (L and T). Primarily, it is important to note that the wave propagation in the assumed range of 0 – 500 kHz is a complex problem, because of the multimodal character of the guided waves. Sixteen modes were obtained from the calculations, however, it was difficult to identify them separately in the experimental maps because of the small differences in wavenumber values and multiple intersections. Nevertheless, the overall view of the 2D-FFT maps corresponds to the shape of the theoretical curves. As a result of the SAFE approach, there are mixed symmetric, antisymmetric and shear horizontal modes (there is no simple way to decouple the problem of propagating Lamb and SH waves). The fundamental S0, A0, and SH0 modes were marked in all subfigures. Firstly, it is important to note that there is a significant discrepancy between the 2D-FFT maps obtained from the processing of signals collected on steel and CFRP surfaces. From the steel side (left column in Figure 6ab), the maps are similar in both L and T directions. This is because the steel plate was relatively thick, which may have impeded propagation through the whole thickness of the joint. The curves are similar in value to the ones obtained for the single steel plate (cf. Figure 4), however, the appearance of higher modes is demonstrably shown by the significant disturbance of the maps, especially in L direction. The S0 and A0 modes were not detected in a higher frequency range (above approximately 250 kHz), SH0 mode was also not present in both directions. Turning to the curves

registered on the CFRP side (right column in Figure 6ab), the presence of A0 mode in a high frequency range (above 250 kHz) was evident. In the L-direction, the A0 mode could be misinterpreted as a SH0 mode which was not actually present. The S0 mode was detected in T-direction, which may have been caused by the presence of carbon fibres. This stays with the agreement with the CFRP curves (cf. Figure 5), for which S0 mode was also observed only in T-direction curves.

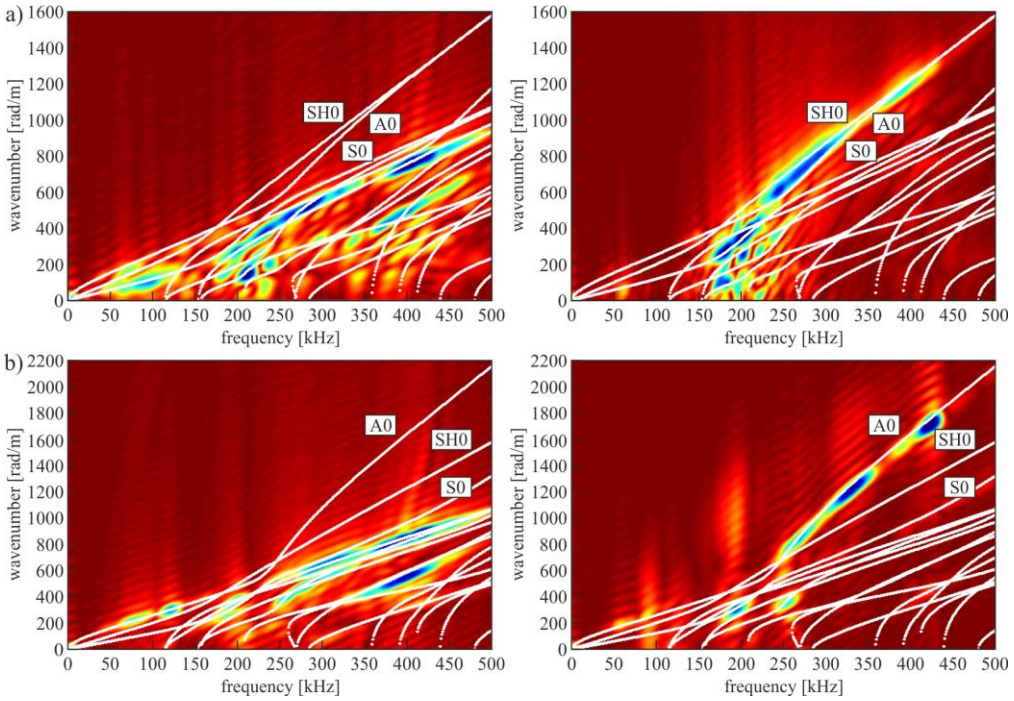

Figure 6. Experimental (coloured maps) and theoretical (white lines) dispersion curves for intact joint #0 (experimental curves measured at steel and CFRP sides in left and right columns, respectively): a) L-direction; b) T-direction

The interpretation of dispersion curves can be very helpful in the determination of the appropriate excitation parameters [38]. It is well known that the interpretation of wave propagation with lower frequencies is far easier since a small number of wave modes are simultaneously present. On the other hand, the lower wave frequency, the poorer resolution of damage visualization, which is connected with the increase in wavelength. Thus, it is essential to choose an excitation frequency that is high enough to give efficient results and simultaneously is relatively low to excite only a few wave modes. For the analyzed joint #0, two fundamental modes S0 and A0 propagates in the frequency range up to about 115 kHz. Based on this fact, the excitation frequency for damage detection and visualization was assumed to be equal to 100 kHz (cf. Section 2.2.2). What is noteworthy, due to the fact of registering signals on CFRP surface, the difference between wave propagation in the area of damage (single-layer CFRP plate) and the joint (three-layer waveguide) can be the basis for distinguishing between these two media, leading to a successful damage identification and visualization. The comparison between the dispersion curves for joint #0 and CFRP plate #G is presented in Figure 7. There is a clear distinction between the curves for a chosen frequency. It corresponds to the difference in wave velocity which is a significant factor affecting the energy of propagating waves. On this basis, it can be stated that damage detection with WRMS (which is connected to wave energy) should be efficient.

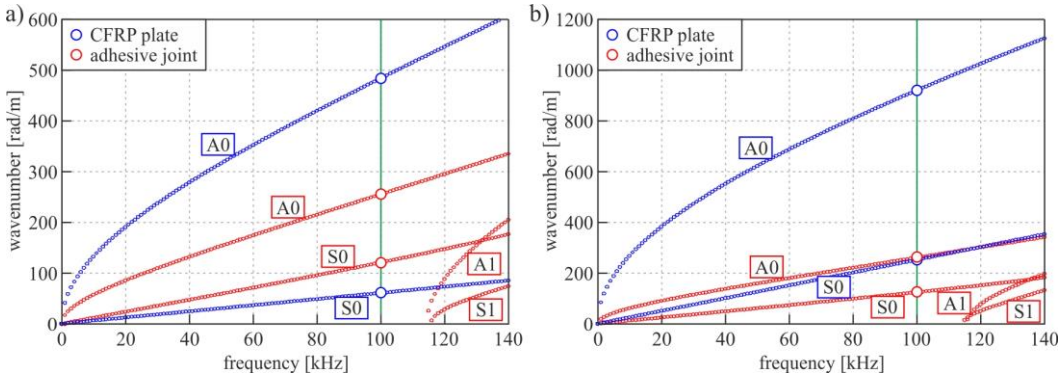

Figure 7. Comparison of dispersion curves for CFRP plate #G and intact joint #0: a) L-direction; b) T-direction

4.2. Damage detection

4.2.1. Damage identification

The diagnostics of analyzed specimens was divided into two stages (cf. Figure 1, steps 2 and 3). The first one of those is damage identification, focused on providing information about the presence of damage. The signals collected in control points P1 and P2 were engaged (see Figure 3c). This allowed stating that damage identification can be done in a low-time cost measurement. Firstly, the WRMS values were calculated for signals from both control points in all joints #0 – #5 and then normalized with respect to the WRMS in control point P1. This operation allowed treating the WRMS in point P1 as a reference and the value in point P2 as an indicator, giving information about the change of the wave energy which is sensitive to damage in the joint (it is expected to increase in the presence of any damage). The WRMS ratio was calculated for point P2 by dividing the values in all joints #0 – #5 by the WRMS value for intact joint #0, thus an increase of WRMS ratio can inform about potential defects. This assumption can be made taking into account the damping of adhesive. The presence of epoxy in areas with good adhesion reduces the signal amplitude, thus the damaged regions (without adhesive) are characterized by the higher values of WRMS (which is actually an energy-based damage indicator). It is a well-known fact that WRMS calculation parameters (such as the time of averaging T_e and weighting factor described with the power m, see Section 2.4) have a significant influence on the obtained WRMS values, thus there is the need to determine the optimal values. For this reason, several calculations were conducted for a set of parameter values (m was assumed in the range of 0 – 5 with a step of 0.05 and T_e varied between 0.3 ms to 3.1 ms with a step of 0.05 ms). A linear relationship between WRMS ratio and the percentage of damage surface for partially damaged joints (#1 – #4: 10%, 20%, 50%, 80%, respectively) was assumed. Two-dimensional optimization in the m-T_e domain was performed with a criterion of maximization of the linear correlation coefficient r (using Pearson's definition). The variation of r with respect to m and T_e is presented in Figure 8a. It is important to note that the calculated surface did not have a trivial shape. The low values of r were obtained mainly for lower values of T_e, however, the higher ones were also not very efficient. The global maximum (marked in the figure) of r was obtained for the optimal values of the calculation parameters: $m_{opt} = 0.85$ and $T_{e,op} = 2.1$ ms ($r = 1.000$). Remarkably, the maximum was not sharp, and many more parameter pairs in the adjacent

area had a similar value of r. For this reason, it can be assumed that a series of parameter pairs can give results with comparable efficiency. The threshold $r_t = 0.98$ was assumed to establish the range of possible efficient parameter pairs. It is the inner surface of the irregular shape area marked with a red dashed line in Figure 8a. Any combination of parameters from this surface is expected to provide a useful damage visualization.

To reveal the differences in the correlation coefficient r between different pairs of parameters, the relations between WRMS ratio and the level of damage are presented for different m values (with constant $T_{e,opt}$, Figure 8b) and for different T_e values (with constant m_{opt}, Figure 8c). The optimal result is presented with a red line in both charts, showing a clear linear relationship. It is evident that there is no linear relationship observed between the WRMS ratio and the level of damage for calculation parameters with values distant from the optimal. It is, however, essential to note that there are values for which the relationship is close to linear, which stays in agreement with the conclusions made based on the interpretation of the surface in Figure 8a. What is also important to clarify, the intact joint #0 does not satisfy the linear relation because it has no damage, thus there is no factor causing the disturbance in wave propagation (in fact, WRMS increase) and it should not be considered with damaged joints. Another exception is sample #5 that is also out of relation. This specimen, being a single CFRP plate is actually an intact specimen because the excitation and control points are placed all on the same surface, thus no significant increase in WRMS can be observed between control points P1 and P2. It is also important to note that it has WRMS ratio similar to the intact joint #0 (lower or higher, depending on the calculation parameters), which testifies the appropriateness in the preparation of specimen #0.

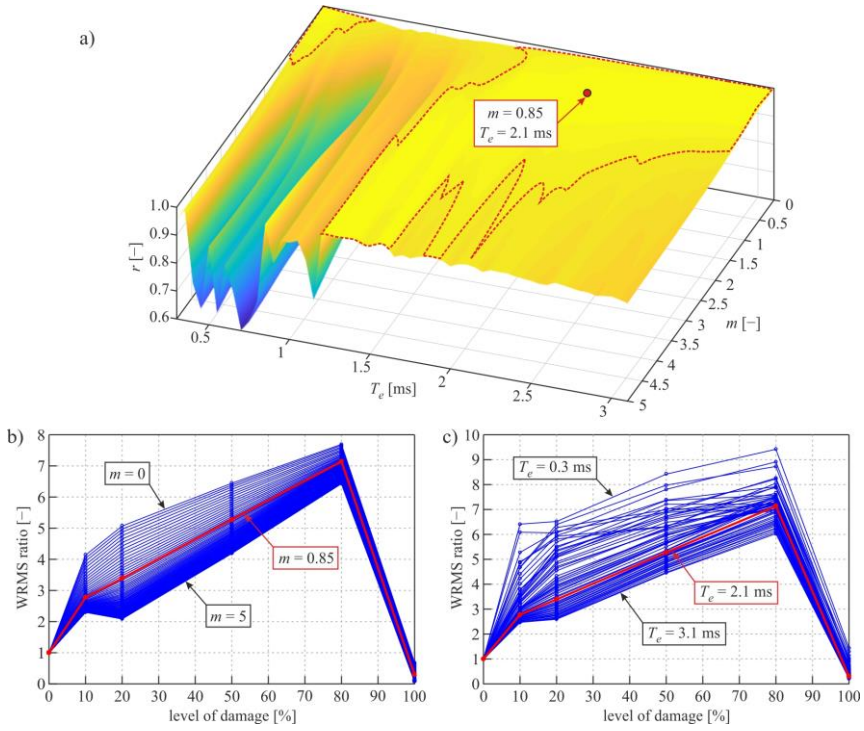

Figure 8. Determination of the optimal calculation parameter based on the designed level of damage: a) linear correlation coefficient in regard to time of averaging and power of weighting factor; b) WRMS ratio for different powers of weighting factor; b) WRMS ratio for different averaging time

To sum up the above analysis, the guided wave measurements in a small number of points, supported with WRMS calculations can be successfully used in the damage identification of defects. However, it is important to note that a full separation is not clearly detected. It is expected that once the optimal parameters are determined, they can be used for damage identification of a random defect. The initial analysis of parameters can be conducted based on a series of physical models with intentionally prepared damage (like in the current research) or in the way of numerical simulations.

4.2.2. Damage visualization using WRMS maps

For damage visualization, the WRMS ratios of wave signals collected in all points in the scanned area (cf. Figure 3c) were calculated. Taking into account that WRMS values are normalized with respect to the value calculated in the control point P1, the mutual scale for all maps was assumed. The results of WRMS calculations for different pairs of calculation parameters are presented in Figure 9. Firstly, the WRMS maps for the optimal parameters (m = 0.85 and T_e = 2.1 ms resulting in r = 1.000) are presented in Figure 9a. It is visible that there are some dispersed defects in joint #0 designed as intact. This may have occurred due to the possibility of the fact that the quality of the contact between the adherends and the adhesive film was not unified (e.g., the adhesive could not be perfectly spread on the joint). According to the dispersion curves discussed in Section 3.1, this may have affected the shape of some modes (e.g., A0 is slightly shifted in the curves determined in T-direction from CFRP side). However, the values are not significant, so the joint can still be assumed as intact. For the damaged joints #1 – #4, the WRMS values are significantly higher when compared with the area of the properly prepared joint. The clearest increase of WRMS in the debonded area is obtained for joint #1 and it slightly decreases with the size of the defect, however, it is still really efficient for the greatest damage in sample #4. These changes are the result of the fact that the greatest damage area, the less reflections the wave experiences during the assumed time of propagation. What is important for joints #1 – #3, there are some additional unintentional damage areas aside from the designed damage. The reason for this fact may be the shrinkage of the adhesive during the curing process. It creates the need for correction of the above-conducted optimization, which will be discussed in the further part of the study. The separate composite #5 has no visible defects because it should be actually treated as the one without damage. The conclusions from the interpretation of the maps agree with the ones obtained during the damage identification step. Figure 9b shows the WRMS maps for another pair of parameters giving the correlation coefficient above the assumed threshold (m = 0.60 and T_e = 1.6 ms, r = 0.984). The efficiency of visualization is comparable to the one obtained for optimal values. To prove that the proposed optimization method is justified, two examples of WRMS visualizations for pairs of parameters that result in correlation coefficients below the threshold are presented. Figure 9c presents the maps calculated for m = 3.00 and T_e = 0.7 ms (r = 0.729). The visualization of the defects is not as clear as for the above-discussed pairs, especially for specimen #4 with the greatest damage. What is more, the sample #5 seems to be partially damaged, which is the result of the fact of the low value of time of averaging. Another example (Figure 9c, m = 5.00, T_e = 3.1 ms, r = 0.950) is also not efficient, despite

the relatively high value of r. The visualizations are even less clear, only #3 has a visible defect, while the others have barely visible damages. Moreover, artificial defects are visible in joint #5.

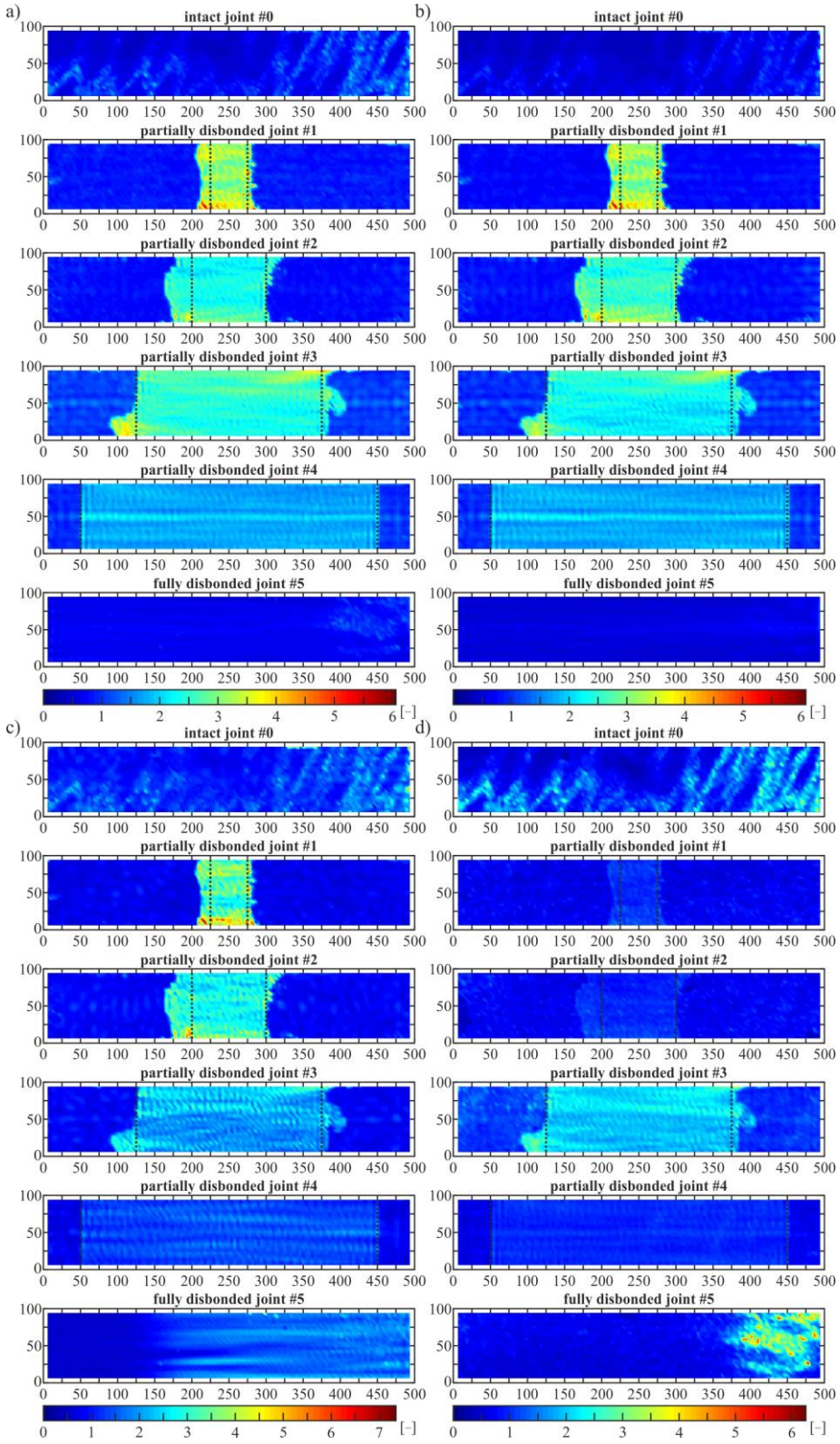

Figure 9. WRMS maps (dimensions in [mm]) for all joints for different pairs of calculation parameters (weighting factor exponent m and time of averaging T_e) with calculated correlation coefficient: a) m = 0.85, T_e = 2.1 ms, r = 1.000 (optimal pair); b) m = 0.60, T_e = 1.6 ms, r = 0.984; c) m = 3.00, T_e = 0.7 ms, r = 0.729; d) m = 5.00, T_e = 3.1 ms, r = 0.950

4.2.3. Statistical analysis – WRMS histograms

Additional information about the efficiency of the prepared WRMS maps can be provided by tools of statistical analysis, i.e., histograms. The WRMS values calculated for all points in the scanned area are treated as a series of scalar values for which a histogram can be calculated such as a probability distribution fitted. Firstly, the mean value and standard deviation of the set of values were calculated. The extreme values (extremely high and low) that may disturb the histograms were excluded from further calculations using the three-sigma rule, which allows omitting the values differing from the mean with more than three standard deviations (leaving about 99.7% of values). Secondly, the *histfit* function from Statistics and Machine Learning Toolbox in MATLAB® was used to plot the probability density functions. The results of the calculations for two pairs of WRMS calculation parameters are presented in Figure 10. The optimal set of parameters was used to prepare the histograms that are presented in Figure 10a. The intact joint #0 is characterized by the unimodal distribution, which shows that there is a single characteristic mode value describing the map (WRMS ratio of about 0.5 in the peak). However, the mode is not symmetric, it is developed in the direction of higher values, which creates a possibility of revealing a weak (not very clear) disbond. This conclusion agrees with the fact that there is unintentional dispersed damage in the joint (cf. Figure 9). The partially damaged joints #1 – #4 are characterized by evident bimodal distributions. The modes with lower values correspond to the undamaged parts of the joints, whereas the modes with higher values are connected to the defects. The intact mode in damaged samples has a higher value (between 0.8 and 0.9) than the intact mode for joint #0, which allows stating that the presence of the defect influences the WRMS values in the undamaged area. It can be observed that the greater the damaged surface, the more clear is the defect mode in comparison with the intact mode. What is more, the damage mode value decreases with the surface of the damage (from about 3.0 for joint #1 to about 1.4 for joint #4). It shifts to the intact mode, which is also observed in the WRMS maps (cf. Figure 9), where the most clear defect visualization was obtained for joint #1. For joints #1 and #2 the damage mode (its integral) is smaller than the intact one, for joint #3 the two modes are comparable, whereas for joint #4 the defect mode is demonstrably greater than the intact one. This corresponds to the ratio between good adhesion and damaged areas of the joints. The sample #5 has a unimodal distribution, a single symmetric mode can be observed due to the fact that there is no actual damage. The histograms for a pair of calculation parameters that gives $r = 0.950$ (denoted as not efficient) are presented in Figure 10b. The histogram for intact joint #0 is similar to the one obtained for the optimal pair of parameters. What is noteworthy, the histograms for partially damaged joints #1 – #2 present unimodal distributions. However, the asymmetry of the histograms allows stating that there are some weakly detectable disbonds. This agrees with the previously discussed visualizations (cf. Figure 9d). The joints #3 – #4 are described by bimodal distributions. The histogram for joint #3 presents the clear bimodality (the WRMS map also had a good quality), whereas for joint #4 it is not as evident (the map was not as efficient). An interesting fact can be observed for the sample

#5 which has a unimodal distribution, however, some additional higher values with no modal character are present. This clearly corresponds to the artificial damage observed in WRMS maps.

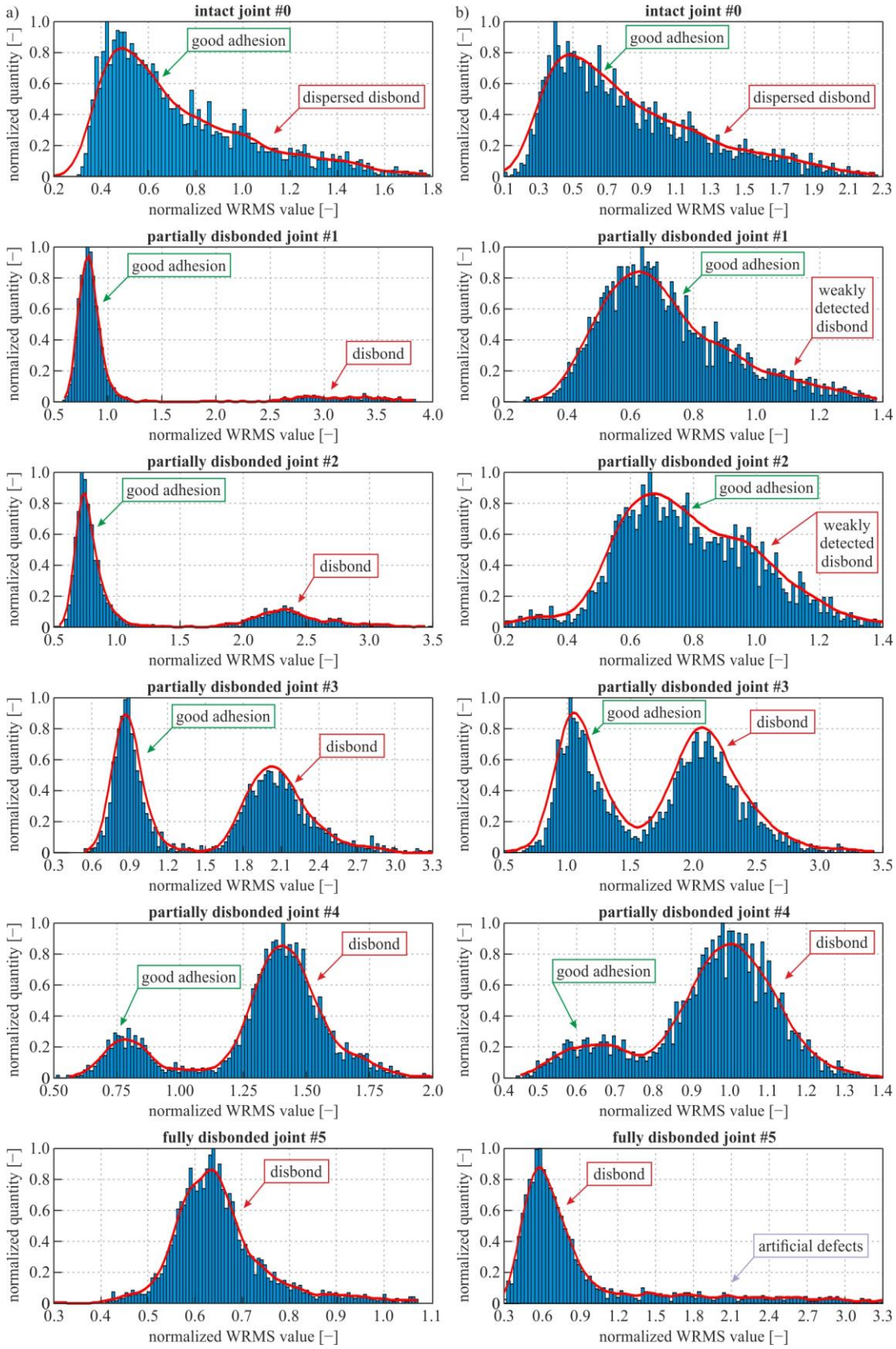

Figure 10. WRMS histograms for damage visualization maps for all joints: a) T_e = 2.1 ms, m = 0.85 (optimal pair, r = 1.000); b) T_e = 3.1 ms, m = 5 (r = 0.950)

The histograms for partially damaged joints #1 – #4 (with optimal calculation parameters) can be used to determine the actual level of damage based on the real defect surface. In this case, the peak values of both good adhesion and damage modes were read from probability distribution functions. The mean value of these two was then calculated to be treated as the limit between the values characterizing the intact and damaged parts of specimens. The number of values above the limit were counted and used for calculation of the corrected defect area (Table 2). It is clear that for joints #1 – #3 the actual damage surface is greater than the designed one (which is visible in the WRMS maps, cf. Figure 9). For the joint #4, the actual damage is equal to the designed one. To better show the results of calculations, the damage visualizations are presented for specimens #1 – #4 in Figure 11. The maps present binary images of defects (black areas denote the defects). The maps agree with the WRMS maps.

Table 2. Estimated level of damage based on WRMS histograms

Value	#1	#2	#3	#4
Good adhesion mode	0.812	0.748	0.878	0.782
Damage mode	2.865	2.343	2.057	1.402
Limit between modes	1.838	1.546	1.468	1.092
Estimated level of damage	15%	27%	55%	80%

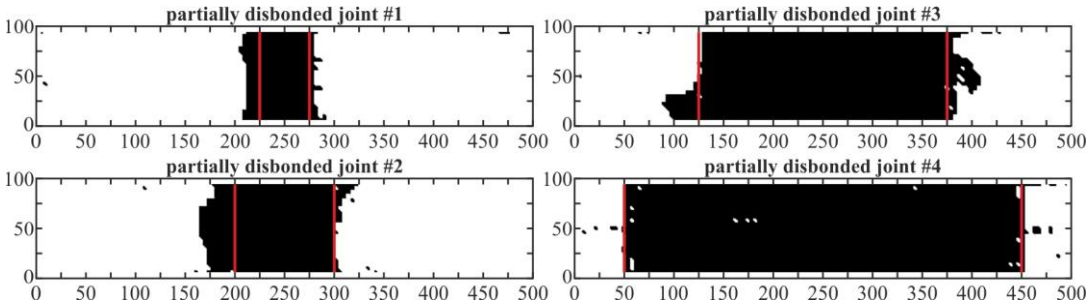

Figure 11. Damage maps for partially damaged joints #1 – #4 (dimensions in [mm])

4.2.4. Updating WRMS damage images

Having the corrected values of the level of damage, the optimization of WRMS calculation parameters was done again to verify the previous calculations (based on the designed values). The results of the calculation of Pearson's correlation coefficient r with respect to time of averaging and weighting factor are presented in Figure 12, altogether with the area of r above the established threshold $r_t = 0.98$. The obtained function does not differ significantly from the one calculated for the designed levels of degradation (cf. Figure 8). The lowest values of the correlation coefficient are obtained for low and high times of averaging. The corrected optimal pair of calculation parameters is $m_{opt,c} = 0.90$, $T_{e,opt,c} = 1.7$ ms. The previously determined optimal values are included in the surface of efficient pairs of calculation parameters with the close to the unit, i.e., $r = 0.998$. The new optimal pair of parameters was verified by the calculation of WRMS maps (Figure 13). The results are comparable in efficiency with the maps for the previously discussed pairs (cf. Figure 9). This allows stating that the actual levels of damage and the designed ones are not significantly different.

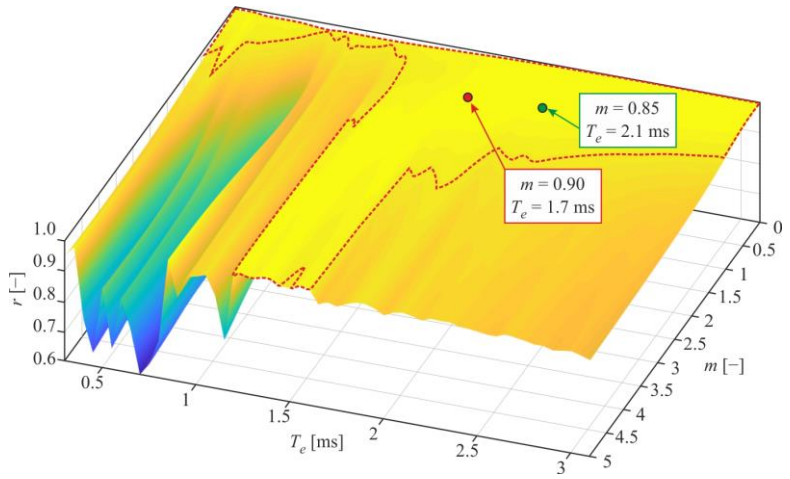

Figure 12. The linear correlation coefficient regarding time of averaging and power of weighting factor for the determination of optimal WRMS calculation parameters based on the actual level of degradation

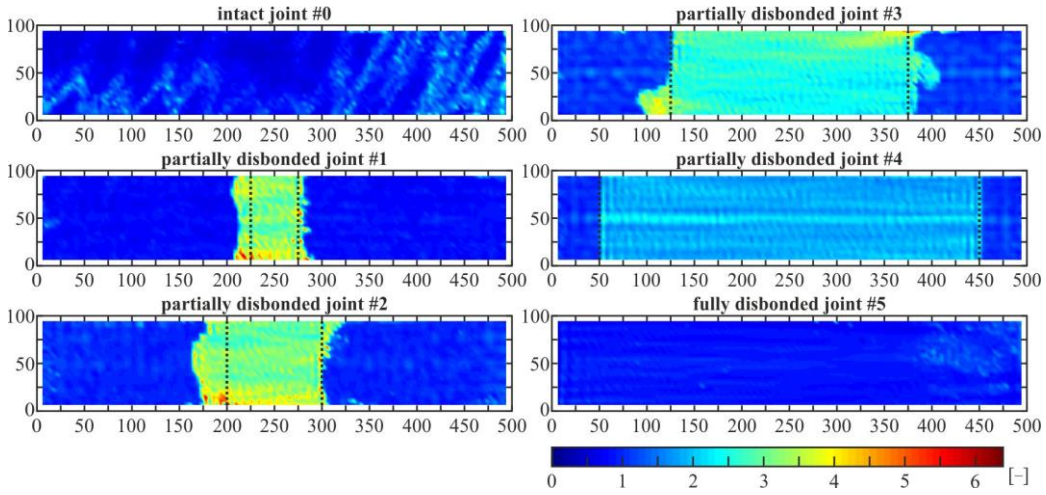

Figure 13. WRMS maps (dimensions in [mm]) for all joints for the optimal pair of calculation parameters based on the actual level of damage, m = 0.90, T_e = 1.7 ms, r = 1.000

4.2.5. Experimental verification of results obtained

To verify the effectiveness of the proposed damage imaging algorithm, the prepared joints #1–#4 were visually assessed. The parts of the samples were detached by hand with the support of a steel spatula to reveal the true shape of the defects. The photographs of the separated adherends are shown in Figure 14. It is clearly visible for all samples that the adhesive remained entirely on the steel plate. This may have resulted from the fact that the steel-adhesive contact is stronger than CFRP-adhesive, because the CFRP plate has fibres that can be separated individually from the rest of the element (what can actually be observed in the photographs). The area of the true damage (white line) is greater than the designed one because there are some unintentionally produced defects, as it was mentioned analysing the previously discussed WRMS maps. It is obvious for all samples #1–#4 that the shape of the true defect is similar to the one presented in damage images in Figure 11. To verify the results quantitatively, the photos of the damaged adherends were processed in ImageJ software [60]. The pictures were first scaled to show the real dimensions of the specimens, i.e. the ratio px/mm was established by the known

length and width of the sample. Then, the parts of defects captured by scanning (red areas) were digitally measured. The gained values were divided by the entire area of scanning (488 × 88 mm^2) to obtain the percentage of damage. The results of the calculations are presented in Table 3. The obtained true level of damage was compared to the one estimated with the proposed algorithm (see Table 2), giving the relative errors up to a few percent. Thus, it can be stated that the proposed damage imaging algorithm allows to determine with sufficient accuracy the size and shape of the defects in adhesive joints.

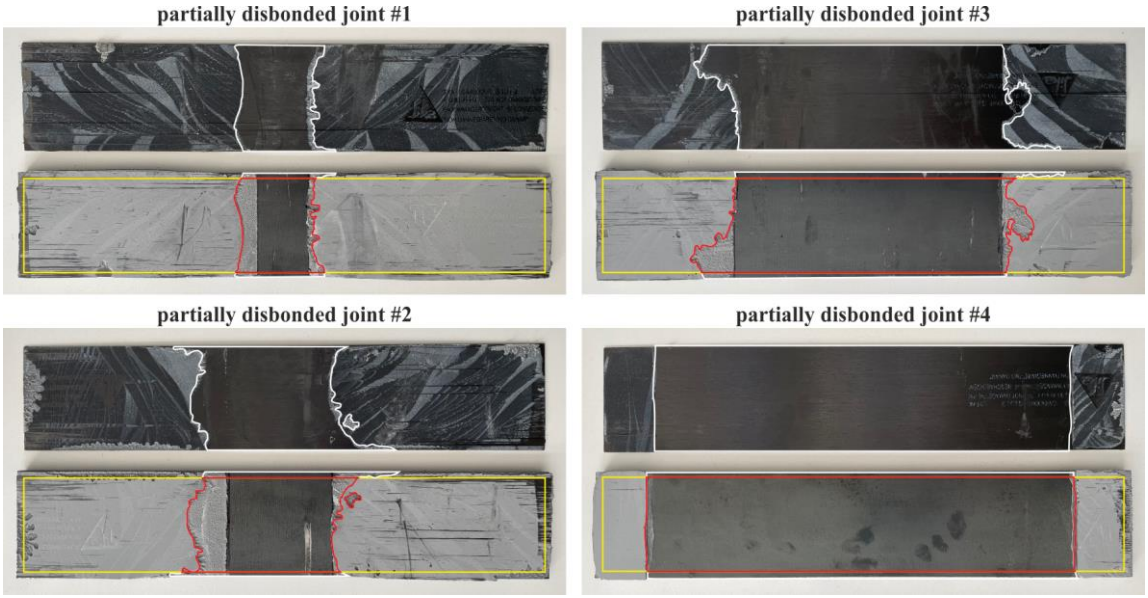

Figure 14. Photographs of the examined joints after disconnection (white line – true defect area, yellow line – scanning area, red line – true defect surface in the scanning area)

Table 3. Verification of estimated level of damage based on experimental examination

Value	#1	#2	#3	#4
Are of defect [mm^2]	6 217	11 867	24 161	34 984
True level of damage	14%	28%	56%	81%
Estimated level of damage	15%	27%	55%	80%
Percentage error of estimation	7.1%	3.6%	1.8%	1.2%

5. Conclusions

In this paper, the condition assessment of steel plates strengthened with adhesively bonded CFRP laminate was carried out by guided wave propagation. The three-stage algorithm for damage imaging was developed. The experimental studies aimed at damage imaging based on weighted root mean square calculations supported with statistical analysis. A description of wave propagation phenomena in the considered three-layer joint and its components was presented to determine the excitation frequency for the guided wave-based damage visualization.

The damage regions were successfully identified and visualized using WRMS maps prepared for guided wave signals. The assumption of linearization between the WRMS value and the level of damage was proved to be effective in the determination of optimal values of WRMS calculation parameters. The

proposed WRMS-based damage imaging allowed visualizing defects intentionally introduced in adhesive joints, as well as unintended ones. The strong impact of WRMS calculation parameters on the efficiency of the obtained damage images was observed. The usefulness of WRMS histograms for the calculation of the actual level of damage was confirmed. The results obtained were successfully verified by visual inspection of the samples after separation.

The proposed three-stage approach has the potential for use in non-invasive diagnostics of large-scale engineering structures. In the first stage (damage identification), a structure should be divided into smaller segments that can be tested one-by-one with a small number of measurements. The results can provide information about the presence of defects. If any defects are identified in a specific segment, the second stage (damage visualization) occurs, which consists of scanning the guided wavefield to obtain detailed damage maps. The future work will focus on the further development of the proposed algorithm to be applicable for real-scale engineering elements, e.g., bridge girders.

Acknowledgements

The support of the Faculty of Civil and Environmental Engineering, Gdańsk University of Technology with the grant for young researchers is gratefully acknowledged. The authors would like to thank Sika Poland and Mr Janusz Potrzebowski for providing materials for the research (CFRP laminate and adhesive).

Data availability

The raw data required to reproduce these findings are available to download from https://doi.org/10.34808/kjsd-7m49. The processed data required to reproduce these findings cannot be shared at this time due to technical or time limitations.

References

[1] Jagtap PR, Pore SM. Strengthening of fully corroded steel I-beam with CFRP laminates. Mater. Today Proc., Elsevier Ltd; 2021. https://doi.org/10.1016/j.matpr.2020.12.106.

[2] Peiris A, Harik I. Steel beam strengthening with UHM CFRP strip panels. Eng Struct 2021;226:111395. https://doi.org/10.1016/j.engstruct.2020.111395.

[3] Nhut PV, Matsumoto Y. Experimental analytical and theoretical investigations of CFRP strengthened thin-walled steel plates under shear loads. Thin-Walled Struct 2020;155:106908. https://doi.org/10.1016/j.tws.2020.106908.

[4] Doroudi Y, Fernando D, Hosseini A, Ghafoori E. Behavior of cracked steel plates strengthened with adhesively bonded CFRP laminates under fatigue Loading: Experimental and analytical study. Compos Struct 2021;266:113816. https://doi.org/10.1016/j.compstruct.2021.113816.

[5] Hassan MM, Shafiq MA, Mourad SA. Experimental study on cracked steel plates with different damage levels strengthened by CFRP laminates. Int J Fatigue 2021;142:105914. https://doi.org/10.1016/j.ijfatigue.2020.105914.

[6] Elchalakani M. CFRP strengthening and rehabilitation of degraded steel welded RHS beams

under combined bending and bearing. Thin-Walled Struct 2014;77:86–108. https://doi.org/10.1016/j.tws.2013.12.002.

[7] Kong D, Huang X, Xin M, Xian G. Effects of defect dimensions and putty properties on the burst performances of steel pipes wrapped with CFRP composites. Int J Press Vessel Pip 2020;186:104139. https://doi.org/10.1016/j.ijpvp.2020.104139.

[8] Xie J, Wu C, Gao L, Xu C, Xu Y, Chen G. Detection of internal defects in CFRP strengthened steel structures using eddy current pulsed thermography. Constr Build Mater 2021;282:122642. https://doi.org/10.1016/j.conbuildmat.2021.122642.

[9] Mazurkiewicz Ł, Małachowski J, Damaziak K, Tomaszewski M. Evaluation of the response of fibre reinforced composite repair of steel pipeline subjected to puncture from excavator tooth. Compos Struct 2018;202:1126–35. https://doi.org/10.1016/j.compstruct.2018.05.065.

[10] Schilde K, Seim W. Experimental and numerical investigations of bond between CFRP and concrete. Constr Build Mater 2007;21:709–26. https://doi.org/10.1016/j.conbuildmat.2006.06.006.

[11] Pan J, Leung CKY, Luo M. Effect of multiple secondary cracks on FRP debonding from the substrate of reinforced concrete beams. Constr Build Mater 2010;24:2507–16. https://doi.org/10.1016/j.conbuildmat.2010.06.006.

[12] Gao P, Gu X, Mosallam AS. Flexural behavior of preloaded reinforced concrete beams strengthened by prestressed CFRP laminates. Compos Struct 2016;157:33–50. https://doi.org/10.1016/j.compstruct.2016.08.013.

[13] Akroush N, Almahallawi T, Seif M, Sayed-Ahmed EY. CFRP shear strengthening of reinforced concrete beams in zones of combined shear and normal stresses. Compos Struct 2017;162:47–53. https://doi.org/10.1016/j.compstruct.2016.11.075.

[14] Zhang P, Lei D, Ren Q, He J, Shen H, Yang Z. Experimental and numerical investigation of debonding process of the FRP plate-concrete interface. Constr Build Mater 2020;235:117457. https://doi.org/10.1016/j.conbuildmat.2019.117457.

[15] Hosseini SMH, Duczek S, Gabbert U. Non-reflecting boundary condition for Lamb wave propagation problems in honeycomb and CFRP plates using dashpot elements. Compos Part B Eng 2013;54:1–10. https://doi.org/10.1016/j.compositesb.2013.04.061.

[16] Martínez-Jequier J, Gallego A, Suárez E, Juanes FJ, Valea Á. Real-time damage mechanisms assessment in CFRP samples via acoustic emission Lamb wave modal analysis. Compos Part B Eng 2015;68:317–26. https://doi.org/10.1016/j.compositesb.2014.09.002.

[17] Zhang X, Wu X, He Y, Yang S, Chen S, Zhang S, et al. CFRP barely visible impact damage inspection based on an ultrasound wave distortion indicator. Compos Part B Eng 2019;168:152–8. https://doi.org/10.1016/j.compositesb.2018.12.092.

[18] Sikdar S, Banerjee S. Guided wave based nondestructive analysis of localized inhomogeneity effects in an advanced sandwich composite structure. Compos Part B Eng 2019;176:107195. https://doi.org/10.1016/j.compositesb.2019.107195.

[19] Duan W, Gan TH. Investigation of guided wave properties of anisotropic composite laminates using a semi-analytical finite element method. Compos Part B Eng 2019;173:106898. https://doi.org/10.1016/j.compositesb.2019.106898.

[20] Nakahata K, Amano Y, Ogi K, Mizukami K, Saitoh T. Three-dimensional ultrasonic wave simulation in laminated CFRP using elastic parameters determined from wavefield data. Compos

Part B Eng 2019;176:107018. https://doi.org/10.1016/j.compositesb.2019.107018.

[21] Apalowo RK, Chronopoulos D. A wave-based numerical scheme for damage detection and identification in two-dimensional composite structures. Compos Struct 2019;214:164–82. https://doi.org/10.1016/j.compstruct.2019.01.098.

[22] Sikdar S, Van Paepegem W, Ostachowicz W, Kersemans M. Nonlinear elastic wave propagation and breathing-debond identification in a smart composite structure. Compos Part B Eng 2020;200. https://doi.org/10.1016/j.compositesb.2020.108304.

[23] James R, Giurgiutiu V. Towards the generation of controlled one-inch impact damage in thick CFRP composites for SHM and NDE validation. Compos Part B Eng 2020;203:108463. https://doi.org/10.1016/j.compositesb.2020.108463.

[24] Rozylo P, Debski H. Effect of eccentric loading on the stability and load-carrying capacity of thin-walled composite profiles with top-hat section. Compos Struct 2020;245:112388. https://doi.org/10.1016/j.compstruct.2020.112388.

[25] Mahmoud AM, Ammar HH, Mukdadi OM, Ray I, Imani FS, Chen A, et al. Non-destructive ultrasonic evaluation of CFRP concrete specimens subjected to accelerated aging conditions. NDT E Int 2010;43:635–41. https://doi.org/10.1016/j.ndteint.2010.06.008.

[26] Li J, Lu Y, Guan R, Qu W. Guided waves for debonding identification in CFRP-reinforced concrete beams. Constr Build Mater 2017;131:388–99. https://doi.org/10.1016/j.conbuildmat.2016.11.058.

[27] Liu S, Sun W, Jing H, Dong Z. Debonding Detection and Monitoring for CFRP Reinforced Concrete Beams Using Pizeoceramic Sensors. Materials (Basel) 2019;12. https://doi.org/10.3390/ma12132150.

[28] Wang Y, Li X, Li J, Wang Q, Xu B, Deng J. Debonding damage detection of the CFRP-concrete interface based on piezoelectric ceramics by the wave-based method. Constr Build Mater 2019;210:514–24. https://doi.org/10.1016/j.conbuildmat.2019.03.042.

[29] Kwon OY, Lee SH. Acousto-ultrasonic evaluation of adhesively bonded CFRP-aluminum joints. NDT E Int 1999;32:153–60. https://doi.org/10.1016/S0963-8695(98)00066-8.

[30] Li J, Lu Y, Lee YF. Debonding detection in CFRP-reinforced steel structures using anti-symmetrical guided waves. Compos Struct 2020;253. https://doi.org/10.1016/j.compstruct.2020.112813.

[31] Spytek J, Ziaja-Sujdak A, Dziedziech K, Pieczonka L, Pelivanov I, Ambrozinski L. Evaluation of disbonds at various interfaces of adhesively bonded aluminum plates using all-optical excitation and detection of zero-group velocity Lamb waves. NDT E Int 2020;112:102249. https://doi.org/10.1016/j.ndteint.2020.102249.

[32] Sha G, Xu H, Radzieński M, Cao M, Ostachowicz W, Su Z. Guided wavefield curvature imaging of invisible damage in composite structures. Mech Syst Signal Process 2021;150. https://doi.org/10.1016/j.ymssp.2020.107240.

[33] Żak A, Radzieński M, Krawczuk M, Ostachowicz W. Damage detection strategies based on propagation of guided elastic waves. Smart Mater Struct 2012;21:035024. https://doi.org/10.1088/0964-1726/21/3/035024.

[34] Lee C, Park S. Flaw Imaging Technique for Plate-Like Structures Using Scanning Laser Source Actuation. Shock Vib 2014:725030. https://doi.org/10.1155/2014/725030.

[35] Lee C, Zhang A, Yu B, Park S. Comparison study between RMS and edge detection image

processing algorithms for a pulsed laser UWPI (Ultrasonic wave propagation imaging)-based NDT technique. Sensors (Switzerland) 2017;17. https://doi.org/10.3390/s17061224.

[36] Pieczonka Ł, Ambroziński Ł, Staszewski WJ, Barnoncel D, Pérès P. Damage detection in composite panels based on mode-converted Lamb waves sensed using 3D laser scanning vibrometer. Opt Lasers Eng 2017;99:80–7. https://doi.org/10.1016/j.optlaseng.2016.12.017.

[37] Rucka M, Wojtczak E, Lachowicz J. Damage imaging in Lamb wave-based inspection of adhesive joints. Appl Sci 2018;8:1–9. https://doi.org/10.3390/app8040522.

[38] Wojtczak E, Rucka M. Wave frequency effects on damage imaging in adhesive joints using lamb waves and RMS. Materials (Basel) 2019;12:1842. https://doi.org/10.3390/ma12111842.

[39] Rucka M, Wojtczak E. Measurements of guided wave propagation in CFRP/steel adhesive joints obtained by scanning laser vibrometry [Data set] 2021. https://doi.org/https://doi.org/10.34808/kjsd-7m49.

[40] Tian Y, Shen Y, Qin X, Yu Z. Enabling the complete mode conversion of Lamb waves into shear horizontal waves via a resonance-based elastic metamaterial. Appl Phys Lett 2021;118. https://doi.org/10.1063/5.0032802.

[41] Graff KF. Wave Motion in Elastic Solids. London: Oxford University Press; 1975.

[42] Lowe MJS. Guided Waves in Structures. Encycl Vib 2001:1551–9. https://doi.org/10.1006/rwvb.2001.0173.

[43] Rose JL. Ultrasonic Guided Waves in Solid Media. New York: Cambridge University Press; 2014. https://doi.org/10.1017/CBO9781107273610.

[44] Jones RM. Mechanics of composite materials. Philadelphia: Taylor & Francis; 1999.

[45] Hwang SF, Wu JC, Barkanovs E, Belevicius R. Elastic constants of composite materials by an inverse determination method based on a hybrid genetic algorithm. J Mech 2010;26:345–53. https://doi.org/10.1017/S1727719100003907.

[46] Nayfeh AH, Chimenti DE. Free wave propagation in plates of general anisotropic media. J Appl Mech Trans ASME 1989;56:881–6. https://doi.org/10.1115/1.3176186.

[47] Bocchini P, Asce M, Marzani A, Viola E. Graphical User Interface for Guided Acoustic Waves. J Comput Civ Eng 2011;25:202–10. https://doi.org/10.1061/(ASCE)CP.1943-5487.0000081.

[48] Alleyne DN, Cawley P. A 2-dimensional Fourier transform method for the quantitative measurement of Lamb modes. Proc IEEE Ultrason Symp 1990;2:1143–6. https://doi.org/10.1109/ULTSYM.1990.171541.

[49] Song H, Popovics JS. Characterization of steel-concrete interface bonding conditions using attenuation characteristics of guided waves. Cem Concr Compos 2017;83:111–24. https://doi.org/10.1016/j.cemconcomp.2017.07.001.

[50] Ong WH, Rajic N, Chiu WK, Rosalie C. Determination of the elastic properties of woven composite panels for Lamb wave studies. Compos Struct 2016;141:24–31. https://doi.org/10.1016/j.compstruct.2015.12.017.

[51] Gallina A, Ambrozinski L, Packo P, Pieczonka L, Uhl T, Staszewski WJ. Bayesian parameter identification of orthotropic composite materials using Lamb waves dispersion curves measurement. J Vib Control 2017;23:2656–71. https://doi.org/10.1177/1077546315619264.

[52] Kudela P, Radzienski M, Fiborek P, Wandowski T. Elastic constants identification of woven fabric reinforced composites by using guided wave dispersion curves and genetic algorithm.

Compos Struct 2020;249:112569. https://doi.org/10.1016/j.compstruct.2020.112569.

[53] Kudela P, Radzienski M, Fiborek P, Wandowski T. Elastic constants identification of fibre-reinforced composites by using guided wave dispersion curves and genetic algorithm for improved simulations. Compos Struct 2021;272:114178. https://doi.org/10.1016/j.compstruct.2021.114178.

[54] Wojtczak E, Rucka M. Monitoring the curing process of epoxy adhesive using ultrasound and Lamb wave dispersion curves. Mech Syst Signal Process 2021;151:107397. https://doi.org/10.1016/j.ymssp.2020.107397.

[55] Jothi Saravanan T, Gopalakrishnan N, Prasad Rao N. Damage detection in structural element through propagating waves using radially weighted and factored RMS. Measurement 2015;73:520–38. https://doi.org/10.1016/j.measurement.2015.06.015.

[56] Kudela P, Wandowski T, Malinowski P, Ostachowicz W. Application of scanning laser Doppler vibrometry for delamination detection in composite structures. Opt Lasers Eng 2016;99:46–57. https://doi.org/10.1016/j.optlaseng.2016.10.022.

[57] Tang ZS, Lim YY, Smith ST, Izadgoshasb I. Development of analytical and numerical models for predicting the mechanical properties of structural adhesives under curing using the PZT-based wave propagation technique. Mech Syst Signal Process 2019;128:172–90. https://doi.org/10.1016/j.ymssp.2019.03.030.

[58] Sabbagh J, Vreven J, Leloup G. Dynamic and static moduli of elasticity of resin-based materials. Dent Mater 2002;18:64–71. https://doi.org/10.1016/S0109-5641(01)00021-5.

[59] Jacob GC, Starbuck JM, Fellers JF, Simunovic S, Boeman RG. Strain rate effects on the mechanical properties of polymer composite materials. J Appl Polym Sci 2004;94:296–301. https://doi.org/10.1002/app.20901.

[60] Abràmoff MD, Magalhães PJ, Ram SJ. Image processing with imageJ. Biophotonics Int 2004;11:36–41. https://doi.org/10.1117/1.3589100.